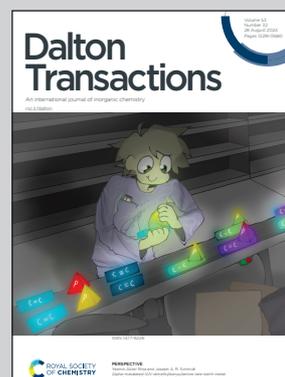**Showcasing research from Professor Ehrenberg's laboratory, Institute for Applied Materials – Energy Storage Systems, Karlsruhe Institute of Technology, Baden-Württemberg, Germany.**

Influence of oxygen distribution on the Li-ion conductivity in oxy-sulfide glasses – taking a closer look
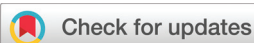
Our work focuses on identifying structure–property relationships in oxygen-substituted Li-thiophosphate glasses. The analysis of $Li_3PO_xS_{4-x}$ glasses, synthesised using two different sets of starting materials, revealed that the distribution of oxygen within the material largely affects the ionic conductivity. At the same total oxygen concentration, structural units containing a high amount of oxygen (PO_4, PO_3S) are more detrimental to the ion conductivity than those with less oxygen (POS_3). Molecular dynamics simulations could confirm the experimental findings.

As featured in:

Dalton Transactions

An international journal of inorganic chemistry

rsc.li/dalton

ROYAL SOCIETY OF CHEMISTRY

PERSPECTIVE

ROYAL SOCIETY OF CHEMISTRY

rsc.li/dalton

Check for updates

Influence of oxygen distribution on the Li-ion conductivity in oxy-sulfide glasses – taking a closer look†

Ramon Zimmermanns, [a] Xianlin Luo,[a] Anna-Lena Hansen, *[a] Marcel Sadowski, [b] Qiang Fu,[a] Karsten Albe, [b] Sylvio Indris, [a,c] Michael Knapp [a] and Helmut Ehrenberg [a]

Lithium thiophosphates are a promising class of solid electrolyte (SE) materials for all-solid-state batteries (ASSBs) due to their high Li-ion conductivity. Yet, the practical application of lithium thiophosphates is hindered by their chemical instability, which remains a prevalent challenge in the field. Oxygen substitution has been discussed in the literature as a promising strategy to enhance stability. Nevertheless, the lack of understanding of the role of synthesis strategy on the resulting structure–property relationship makes it difficult to predict and control the material's behaviour, limiting our ability to fully utilize oxygen substitution as a viable solution. Here, we show that not only the total oxygen content but also the oxygen distribution within the material affects the ion conductivity. By carefully analysing the local structure of oxy-sulfide glasses, we find that few highly oxygenated structural units like $[PO_4]^{3-}$ and $[PO_3S]^{3-}$ are more detrimental to the ionic conductivity than a larger amount of less substituted units like $[POS_3]^{3-}$. Further, we demonstrate how the oxygen distribution is connected to the synthesis in high-energy ball milling by comparing two different sets of precursor materials. The results may explain the deviations in the past literature. The findings should be transferable to other Li-thiophosphate materials and enable more directed design of new materials.

Introduction

Lithium-ion batteries (LIBs) are dominating the markets of portable electronic devices and electric vehicles[1–5] and their market is expected to grow significantly within the next ten years.[6] However, liquid electrolytes used in traditional LIBs, which normally consist of Li salts dissolved in organic solvents, cause serious safety problems regarding flammability and possible leakages.[7,8] All-solid-state batteries (ASSBs) using solid-state electrolytes (SSEs) are proposed to overcome the safety issues of LIBs. SSEs can offer high thermal stability, and enable a simple battery design.[9,10] Moreover, the potential use of Li metal as the negative electrode improves the energy density of ASSBs owing to its high theoretical capacity of

3860 mA h g^{-1}. $Li_2S–P_2S_5$ binary ionic conductors are among the most promising SSEs due to their high ionic conductivity of over 10^{-3} S cm^{-1} at RT.[11–14] Even recyclability has been demonstrated for Li_3PS_4 in recent studies.[15,16] The main drawback of sulfidic SSEs, however, is their high reactivity towards oxidation.

Oxygen substitution is a common approach to enhance the chemical stability of thiophosphate SSEs. Multiple studies report the successful synthesis of oxy-sulfide glasses and glass-ceramics using a variety of different reaction conditions and precursors.[17–25] Two commonly used precursors for oxygen substitution are Li_3PO_4 and Li_2O, which differ mainly in the way oxygen is bound. While Li_3PO_4 is already build-up of tetrahedral units, much like the thiophosphate, these tetrahedra are formed during synthesis when Li_2O is used. The introduction of these compounds has been demonstrated to enhance electrochemical stability and cyclability in ASSBs.[22–24] The tangible influence of oxygen doping on the ion conductivity however is not clear.[26] The parameter space for the synthesis of Li-oxysulfide glasses is immense and different synthesis routes are proposed in the literature. The three most commonly used synthesis routes are solvent-assisted wet chemical synthesis, high-temperature solid-state synthesis, and mechanochemical synthesis in a ball mill. Each synthesis method

aInstitute for Applied Materials – Energy Storage Systems (IAM-ESS), Karlsruhe Institute of Technology (KIT), Hermann-von-Helmholtz-Platz 1, 76344 Eggenstein-Leopoldshafen, Germany. E-mail: anna-lena.hansen@kit.edu
bTechnical University of Darmstadt (TUD), Institute of Materials Science, Otto-Berndt Strasse 3, 64287 Darmstadt, Germany
cApplied Chemistry and Engineering Research Centre of Excellence (ACER CoE), Université Mohammed VI Polytechnic (UM6P), Lot 660, Hay Moulay Rachid, Ben Guerir, 43150, Morocco
†Electronic supplementary information (ESI) available. See DOI: https://doi.org/10.1039/d4dt01132e

comes with its own set of synthesis parameters that can be tweaked. Additionally, various sets of precursors (Li_3PO_4 + Li_3PS_4/Li_2O + Li_2S + P_2S_5/Li_2S + P_2S_5 + P_2O_5) and stoichiometries all affect the properties of the product.[27] Some studies found a maximum in conductivity for small amounts of oxygen substitution, while others found a steady decrease.

At the same time, the reported conductivity values and proposed ideal composition spread over a wide range. Takada *et al.* reported $(1 - x)Li_3PS_4$–xLi_3PO_4 with enhanced conductivity obtained by adding up to 20% Li_3PO_4 *via* a quenching method.[24] Huang *et al.* in contrast prepared amorphous powders $(0.7Li_2S$–$(0.3 - x)P_2S_5)$–xLi_3PO_4 *via* high-energy ball milling, which showed the highest RT conductivity of 1.9×10^{-3} S cm^{-1} with x = 1 mol%.[25] A similar trend was found by Mo *et al.* in $0.95(0.7Li_2S$–$0.3P_2S_5)\cdot0.05Li_3PO_4$ glass electrolyte, where the ionic conductivity, electrochemical stability, and cyclability were improved by doping with Li_3PO_4.[28] More recently, Phuc *et al.* prepared Li_3PS_4–xLi_3PO_4 by liquid-phase synthesis with enhanced conductivity compared to pure Li_3PS_4.[23] The sample with x = 1 mol% has the best stability against Li and the best cycling performance in their report. On the other hand, Trevey *et al.* as well as Tsukasaki *et al.* both found decreasing conductivities when they partially substituted Li_2S with Li_2O using mechanochemical synthesis.[21,22] All these studies lack a deep structural investigation of possible alterations caused by oxygen substitution, although multiple studies on pure Li_3PS_4 indicate, strong correlations between the atomic structure and the ion conductivity.[29–31] The contradictory results of the studies mentioned above, highlight the need for identifying structure–property relationships to develop, a targeted design of materials. Therefore, we aimed for a systematic investigation of *O*-substituted sulfide compounds prepared by mechanical milling.

In the present work, oxy-sulfide glasses with composition $(1 - x)Li_3PS_4$–xLi_3PO_4 ($0.10 \le x \le 0.40$) and $(3 - x)Li_2S$–Li_2O–P_2S_5 ($0.8 \le x \le 2.4$) were prepared by mechanical milling. Exemplarily, two of the most common precursors are used for the synthesis of Li-oxysulfide glasses and glass ceramics to investigate the way that structural units are formed during synthesis. Ball milling is considered to be a promising method for commercialization, because of good scalability,[32] low energy consumption compared to classic high-temperature solid-state synthesis, and reduced environmental input in form of chemical waste compared to wet chemical routes.[33] The structural and electrochemical properties of these oxy-sulfides were characterized by various methods: the atomic structure was examined by X-ray diffraction, synchrotron total scattering, and magic angle spinning nuclear magnetic resonance (MAS NMR) as well as Raman spectroscopy. The chemical composition was verified by X-ray photoelectron spectroscopy (XPS) and energy dispersive X-ray spectroscopy (EDX). The electrochemical properties, meaning the Li-ion conductivity, were measured by electrochemical impedance spectroscopy (EIS). Additionally, the influences of oxygen substitution and distribution within the materials on the ionic conductivity were studied in experiments and by molecular dynamics simulations.

Experimental details

For the pseudo-binary $(1 - x)Li_3PS_4$–xLi_3PO_4 ($0.10 \le x \le 0.40$) series (LIPSO series), the end members were first prepared individually. Li_3PS_4 (LPS) glass was prepared by first mechanical milling of 75 mol% Li_2S (Sigma-Aldrich, 99.98%) and 25 mol% P_2S_5 (Sigma-Aldrich, 99.9%). A batch of about 4 g of this sulfide mixture and 70 g ZrO_2 balls with a diameter of 3 mm were placed in a 45 ml ZrO_2 bowl in an argon-filled glovebox (MBraun, Germany). The mixture was ball milled at 510 rpm for 540 cycles (one cycle equals 5 min milling followed by a 15 min rest for cooling) using the planetary micro mill Pulverisette 7 Premium line (Fritsch, Germany). The total synthesis time was therefore 7.5 d and the total milling time (synthesis time – cooling breaks) was 45 h. After every 72 milling cycles, the milling jars were opened in an argon-filled glovebox to scrap baked powder from the walls of the jar. The glassy Li_3PS_4 was calcined at 250 °C under vacuum in a glass oven (Büchi, Germany) for 2 h and slowly cooled down to RT at a natural rate to obtain β-Li_3PS_4.[34] β-Li_3PO_4 (LPO) was prepared by a wet chemical reaction of 75 mol% 1 M LiOH (Sigma-Aldrich, 99%) and 25 mol% 1 M H_3PO_4 (Carl Roth, 85%). The product was dried at 130 °C for 24 h, ground for 15 min, and then calcined at 300 °C for 16 h in a muffle furnace (P330, Nabertherm). $(1 - x)Li_3PS_4$–xLi_3PO_4 ($0.10 \le x \le 0.40$) was then prepared by mechanical milling of the as-prepared β-Li_3PS_4 and β-Li_3PO_4 using the same process as for glassy Li_3PS_4 for 80 h.

As an alternative approach, $(3 - x)Li_2S + xLi_2O + P_2S_5$ ($0 \le x \le 2.4$) powders (LIO series) were prepared in a one-step mechanical milling process. Li_2S (Sigma-Aldrich, 99.98%), Li_2O (Alfa Aesar, 99.5%), and P_2S_5 (Sigma-Aldrich, 99.9%) were mechanically milled using the same parameters as described above. To enable a reasonable comparison of the products, the milling parameters; rotational speed, cup and ball size, milling time, and ball-to-powder ratios were kept the same for all experiments in both synthesis approaches. After every 72 milling cycles, the milling jars were opened in an argon-filled glovebox to scrap baked powder from the walls of the jar. The milling process was monitored by X-ray diffraction as exhibited in Fig. S5.†

X-ray diffraction (XRD) patterns were collected using an STOE Stadi P powder diffractometer (STOE & Cie GmbH, Germany) equipped with a Mythen 1K detector and Mo $K_{\alpha 1}$ radiation (λ = 0.70932 Å) in Debye–Scherrer geometry using 0.5 or 0.7 mm glass capillaries.

Total scattering experiments were performed at the high-resolution powder diffraction beamline (P02.1) at PETRA-III, DESY (Hamburg, Germany), using synchrotron radiation with a photon energy of 60 keV (λ = 0.2073 Å). The samples were sealed in a 1 mm glass capillary. The diffraction patterns were acquired using a Varex area detector with a sample–detector distance of 300 mm.[35,36] An empty capillary was measured under the same conditions and used for background subtraction. To account for the instrumental resolution, LaB_6 (NIST660c) was measured. The corresponding PDF was calculated using PDFgetX3 with a Q_{max} of 27 Å^{-1}. Q_{damp} = 0.028 Å^{-1} was determined by fitting LaB_6 PDF using PDFgui.[37] Fitted

parameters were scale factor, lattice parameters, isotropic atomic displacement parameters and the particle diameter.

Raman spectra were recorded with a LabRAM HR Evolution spectrometer (HORIBA Scientific, Japan) using a 50× magnification objective, an excitation wavelength of 632.8 nm, and a 600 grooves per mm grating. The samples were measured in sealed glass capillaries with a diameter of 0.5 mm. All Raman spectra were baseline-corrected and normalized using the Horiba LabSpec 6 software.

X-ray photoelectron spectroscopy (XPS) was performed using a K-Alpha spectrometer (Thermo Fisher Scientific, UK) equipped with a micro-focused, monochromatic Al K_α X-ray source (λ = 1486.6 eV) with a spot size of 400 μm. A charge compensation system was employed during the measurement, using electrons of 8 eV energy and low-energy argon ions to prevent localized charge accumulation. Thermo Advantage software was used in data acquisition and processing, as described elsewhere.[38] The analyzer transmission function, Scofield sensitivity factors, and effective attenuation lengths for photoelectrons were applied for quantification.[39] The standard TPP-2M formalism was used for the calculation of effective attenuation lengths.[40] All spectra were referenced to the carbonaceous C 1s peak (C–C/C–H) at 285.0 eV binding energy.

[31]P magic-angle spinning (MAS) nuclear magnetic resonance (NMR) spectra were obtained with an Avance 500 MHz spectrometer (Bruker, Germany) at a field of 11.7 T, corresponding to a resonance frequency of 202.5 MHz. The powder samples were packed into 2.5 mm ZrO_2 MAS rotors in an argon-filled glovebox. For the LIPSO samples, the measurements were performed at a spinning speed of 30 kHz with a rotor-synchronized Hahn-echo pulse sequence, and for the LIO samples, measurements were done at 20 kHz with a single-pulse sequence.

Glass-ceramics (60 mg) were pre-pressed using a pressing die with a diameter of 8 mm *via* a manual hydraulic press (Specac, England) with a pressure of 50 MPa for 10 s at RT. The pellet was then placed in the measurement cell and pressed again with 400 MPa for 2 min. The thickness of the repressed pellet was about 720 μm. All the processes were carried out in an argon-filled glovebox. A detailed description of the in-house cell is displayed in Fig. S1.†[41] All the electrochemical measurements were performed using a multichannel potentiostat VMP3 (Bio-Logic, Germany). Electrochemical impedance spectroscopy (EIS) was conducted on the Li symmetric cell Li/$Li_3PO_xS_{4-x}$/Li with a signal amplitude of 20 mV at frequencies from 1 MHz to 500 mHz. The cells were stored in the glove box for at least two hours before any measurements to ensure a stable interface (see Fig. S2†).

EIS measurements for the $(3 - x)Li_2S + xLi_2O + P_2S_5$ ($0 \leq x \leq 2.4$) powders were conducted in a CompreDrive (rhd instruments GmbH & Co. KG, Germany), using a 6 mm CompreCell with Al_2O_3 core. The sample powder was filled into the cell in an argon-filled glovebox. The powder was pressed inside the CompreDrive with a pressure of 400 MPa for 130 s. If not stated otherwise, the pressure during measurement was set to 100 MPa. The thickness of the pellet was in a similar range as for the measurements in the in-house cell.

Computational methods

Molecular dynamics simulations were performed to investigate Li diffusion coefficients using the LAMMPS[42] code with a machine-learned atomic cluster expansion (ACE, see description further below) potential.[43,44] To this end, amorphous $(1 - x)Li_3PS_4–xLi_3PO_4$ structures with overall compositions between x = 0 and x = 0.25 with 0.05 steps were employed. To investigate the effect of different structural units on the Li diffusion in oxygen-containing structures, we started from a previously generated Li_3PS_4 glass model and prepared supercells containing 2048 atoms.[45] Next, sulfur ions were changed to oxygen in such a way that only PS_4 units and one other type of possible PS_3O, PS_2O_2, PSO_3, or PO_4 units were present.

All simulations were conducted at 500 K with a timestep of 1 fs. For every structure, we ran 5 replica simulations to obtain improved statistics. To properly equilibrate temperature for every replica run, we first ran 50 ps in the microcanonical (NVT) ensemble, followed by 200 ps in the isothermal–isobaric (NpT) ensemble to also equilibrate the cell volume. The last 50 ps of the NpT run were used to obtain an averaged simulation cell, which was then kept fixed for further NVT simulations. To allow for possible further local structural relaxations, another 2 ns of equilibration period were simulated, followed by 8 ns production runs. Ovito[46] was used to analyse the atoms' mean-squared displacement (MSD) according to

$$\text{MSD} = \frac{1}{N}\sum_i^N [r_i(t) - r_i(t = 0)]^2$$

where N is the number of moving particles and $r_i(t)$ is the position of particle i at time t. To improve the statistics, we made use of a sliding window averaging method: with a window length of 4 ns, the MSD was computed for the first part of the production runs and then the start of the next window was shifted by 1 ns until the end of the production run is reached. Therefore, every MSD curve (see Fig. S12†) is obtained as an average of 25 MSD analyses. A linear equation was fitted to the last 3 ns of the averaged MSD to extract its slope dMSD/dt, from which Li tracer diffusion coefficients D can be determined,

$$D = \frac{1}{6}\frac{\text{dMSD}}{\text{d}t}$$

where a three-dimensional diffusion mechanism was assumed. Finally, the conductivity is calculated *via* the Nernst–Einstein equation:

$$\sigma(T) = \frac{\frac{N}{V}D(T)(qe)^2}{kT}$$

where V is the volume of the simulation cell, q is the formal charge of +1 for the Li ions, e is the elementary charge, k is the Boltzmann constant, and T is the temperature.

Fitting the ACE potential relied on data obtained from density functional theory (DFT) calculations. The latter has been performed using VASP[47–50] with projector-augmented

wave (PAW)[51] pseudopotentials and the Perdew–Burke–Ernzerhof (PBE) exchange–correlation potential.[52] The cutoff of the plane-wave basis set was defined to be 600 eV and a k-spacing of 0.25 Å^{-1} was used.

The above-mentioned Li_3PS_4 glass model as well as crystalline β- and γ-Li_3PO_4 have been used as initial training models. Furthermore, these structures were strained, the atomic positions were rattled and/or the oxygen and sulfur content and distribution were changed. Single-point DFT calculations of these structures were used for an initial database to train an ACE potential using the pacemaker[43,44] software, followed by several iterations of active learning (molecular dynamic simulations at temperatures up to 1500 K) to identify unknown atomic configurations. The latter have been added to the database and the ACE potential has been refitted. In every fitting round, four fits with different random seeds were performed and the potential with the lowest root-mean-square errors was used for further steps. The final database contained almost 6000 structures (~1 500 000 atoms in total). The final potential was fitted with a cut-off of 7.5 Å and used a non-linear embedding scheme with 5 terms of power 0.25, 0.5, 0.75, 1, and 2. The fitting results are shown in Table S2† and parity plots of the energy and forces of the training and test set are shown in Fig. S11 and S12.†

Results and discussion

Structure analysis

Oxygen-substituted Li-thiophosphate, $Li_3PS_{4-x}O_x$, has been synthesized using high-energy ball milling. Two different routes have been chosen to investigate the influence of starting materials on the final product. Route one, hereafter referred to as LIPSO starts from Li_3PS_4 and Li_3PO_4. Route two, hereafter referred to as LIO, starts from Li_2S, P_2S_5, and Li_2O. Fig. 1 depicts a schematic overview of the two synthesis routes. The key difference between LIPSO and LIO, as mentioned in the introduction, lies in the fact that for LIPSO, the final structural units like $[PS_4]^{3-}$ or $[PO_4]^{3-}$ tetrahedra are already present in the starting materials, whereas these need to form during synthesis for the experiments in LIO. Since the P–O bond energy is higher than that of the P–S bond, the $[PO_4]^{3-}$ unit should be the thermodynamically most stable tetrahedron in the $PS_{4-x}O_x$ series. Therefore, a low reactivity towards the substitution of an O atom for an S atom in the LIPSO series can be expected. Contrary, in the LIO series all phosphor atoms are initially bound to sulfur, more likely enabling an easy exchange of S for O, possibly leading to more mixed $[PS_{4-x}O_x]^{3-}$ tetrahedra including those with lower oxygen content such as $[POS_3]^{3-}$ or $[PO_2S_2]^{3-}$.

In the LIO series, the XRD reflections from the starting material mostly vanish after about 18 to 24 h and are not observable in the final product. Diffractograms of the starting materials Li_2S and P_2S_5 can be found in Fig. S4(a).† "As reported by Luo,[53] in the LIPSO series, the diffractograms clearly show remaining Li_3PO_4 even after 49 h total milling time while the mechanically softer Li_3PS_4 has been amorphized, see Fig. 2(a and b)."

Rietveld refinement of the crystalline LPO phase of LIPSO samples was carried out to estimate the crystallite size (see Fig. S6†). The amorphous LPS phase was not considered for the refinement and instead modelled as the background. The crystallite size slightly increases from 23 nm for 10% LPO content to 49 nm for 15% LPO content, then steadily decreases with increasing oxygen content to 16.6 nm for the sample with 40% LPO. However, the XRD patterns do not reveal insights into the atomic structure of an amorphous phase, a slight shift of the two broad humps to higher angles and an overall
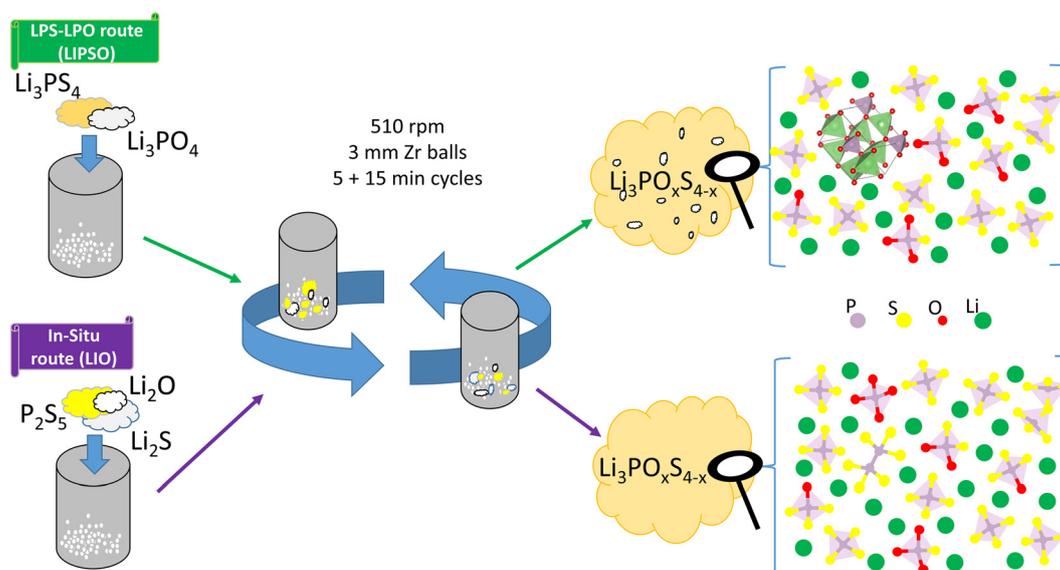

Fig. 1 Schematic description of both experimental series, LIPSO and LIO, and the results of the structural analysis.
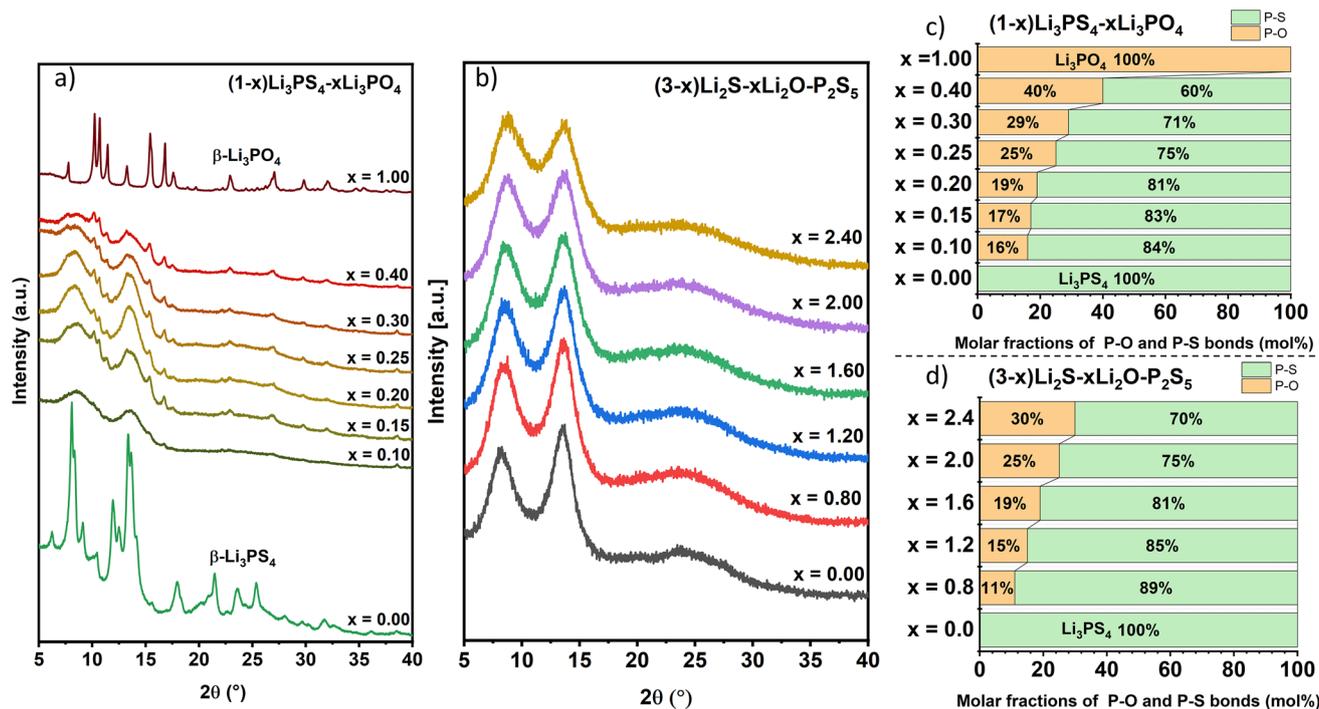
Fig. 2 (a and b) X-ray diffractograms of LIPSO (a) and LIO (b) series. (c and d) Fraction of P–O and P–S bonds in the materials from LIPSO (c) and LIO (d) series, showing the equivalence of both experimental series (a and c taken from Luo 2022).[53]

broadening with increasing oxygen content indicate a shrinkage of the unit cell parameters and an increase of disorder. While the broadening can be observed in both series LIPSO and LIO, the shift to higher angles, hence a shortening of unit cell parameters, seems more pronounced in LIO. The shrinkage can be explained by the difference in P–S and P–O bond lengths of 2.05 and 1.54 Å, respectively.[54] Hence, a more pronounced shrinkage could indicate a better mixing of different $[PS_{4-x}O_x]^{3-}$ tetrahedral species in the LIO series.

XPS measurements were carried out on all samples to obtain chemical information about the materials. Fig. S7(a)† exemplarily displays the XPS wide-scan surveys of both starting materials and the milled oxy-sulfide mixtures for the LIPSO series. Except for the typical carbonaceous contamination at the surface, all expected photoelectrons were detected in all samples. In order to quantify the oxygen content, high-resolution P 2p spectra were collected from starting materials and all oxy-sulfide mixtures (Fig. S7(b)†). Molar fractions of P–O bonds for all milled mixtures were calculated and presented in Fig. 2(c and d). The values of the molar fractions are very close to the desired values, except for the LIPSO sample with $x = 0.10$. The excess P–O bonds in this sample may arise from surface oxidation. The XPS analysis therefore confirms the correct weighing and mixing of starting materials and ensures that the total oxygen concentration is equal for the respective samples in both synthesis routes.

As we will see further below, however, it is not only the total oxygen concentration that determines the ionic conductivity. Therefore, more information on the local structure is needed.

To investigate the local structure, a set of analytic techniques was employed to reach a better understanding of the material's structure and composition.

Pair distribution function (PDF) analysis is a powerful tool to gain insight into the real local structure of crystalline and amorphous materials. The radial distributions $G(r)$ are displayed in Fig. 3(a and b). The low r region of all PDFs up to around 8.5 Å is dominated by the thiophosphate phase, all visible peaks can be attributed to P–S or S–S pairs. Fig. 3(c) shows the low r region of LIO samples, which is indistinguishable from the same region of LIPSO samples. The first peak at 2.05 Å corresponds to the P–S pair, and the second peak at 3.35 Å fits the shortest S–S distance, which is the distance between two sulfurs within one $[PO_xS_{4-x}]^{3-}$ tetrahedron. All peak assignments and a zoom-in on the low r region of LIPSO can be found in Fig. S9.† From the two distances, we can calculate the S–P–S bond angle to be 109.56°, which corresponds well to the ideal tetrahedron angle of 109.57°. Hence, we can conclude from the first two peaks of the PDF that all the glasses are mainly composed of uniform $[PS_4]^{3-}$ tetrahedra, as has been reported in other studies.[27,34,55,56] The connectivity of these tetrahedra is however not obvious, as isolated tetrahedra and corner or edge-sharing tetrahedra would produce a similar PDF as long as the bond length and angles do not change. The connectivity information is encoded in the ratio of peak integrals for the P–S and S–S peaks.

While the coordination number for P–S should always be equal to the number of S in the formula unit (between 4 and 2.8 depending on oxygen substitution), the coordination
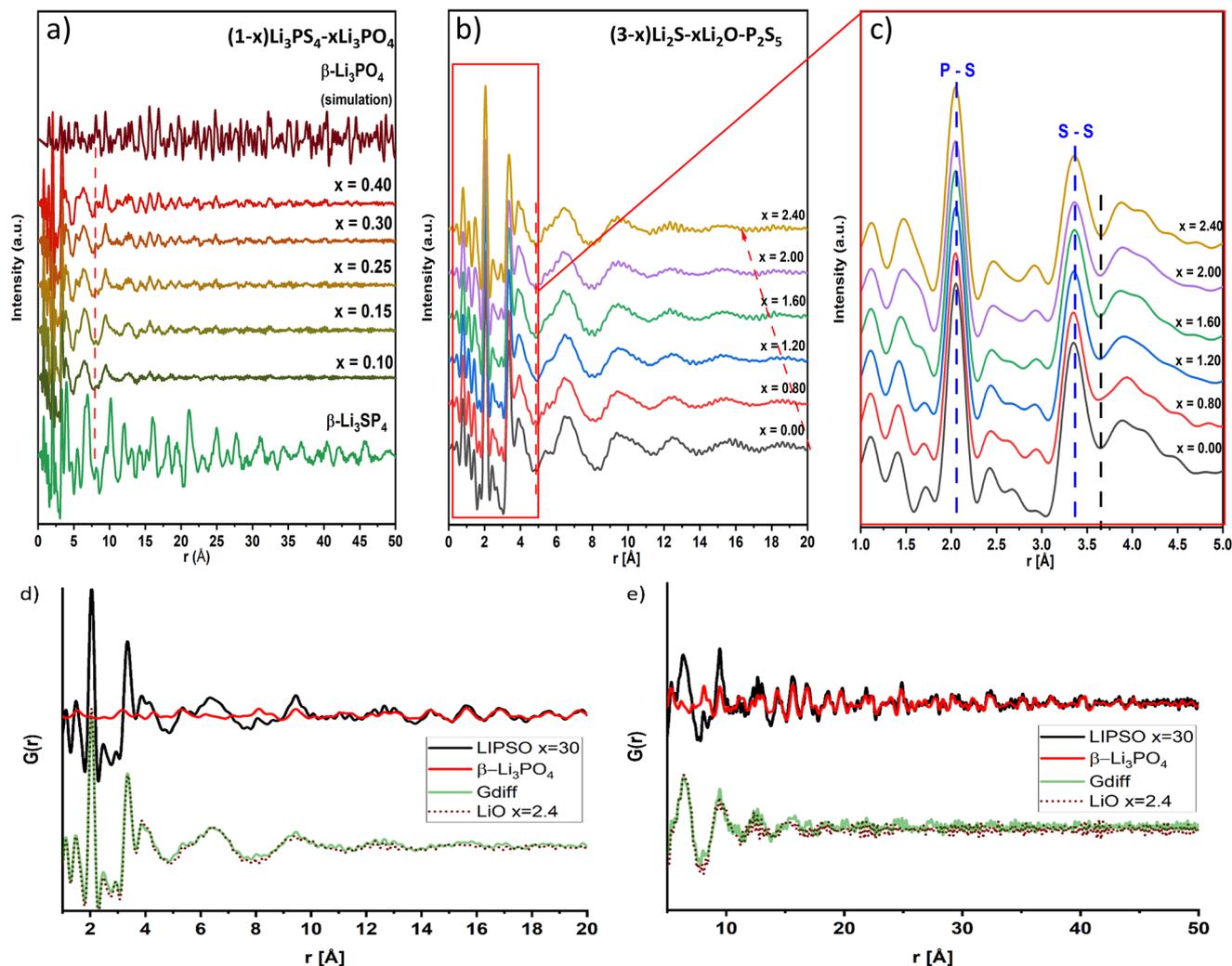
Fig. 3 (a) PDFs of LIPSO with simulated PDF of β-Li$_3$PO$_4$. (b) PDFs of LIO, the dashed red line marks the end of strong short-range order and the dashed red arrow marks the decrease of correlation length with higher oxygen content. (c) Zoom in on the short-range region of the PDFs in (b). (d and e) PDF of LIPOS sample with 30% LPO (black) with PDFgui fit of the β-LPO phase (red) and the difference curve (green) compared to the LIO sample with the same oxygen content (brown, dotted).

number for S–S would be between 3 and 1.8 for only isolated, and 6 to 3.6 for only corner-sharing tetrahedra. The structure exhibits two distinct S–S distances for inter and intra-tetrahedral S–S pairs. In the PDF the intra-tetrahedral S–S pairs are represented by a sharp peak at 3.35 Å and the inter-tetrahedral S–S pairs by a broader peak around 3.85 Å. The overlap of these two peaks makes the integration difficult and less precise. In addition, any impurities with other coordination environments would also change the peak integrals. For this reason, the data do not allow a meaningful evaluation of the coordination numbers. For the LIO samples (see Fig. 3(b)) the PDF contains only broad features for $r > 5$ Å and is damped out quickly. The black line in Fig. 3(c) marks the transition from intra to inter-tetrahedra correlations. The transition can be identified by the sudden change in peak width. All peaks at low r are much sharper due to correlative motion of the atoms within a tetrahedron. For different orientations of tetrahedra

with respect to each other, there are many possible configurations; hence, the corresponding distances are less defined. These oscillations at mid and high r ($r > 5$) signify a limited ordering in the distance between nearest $[PO_xS_{4-x}]^{3-}$ tetrahedra, most likely as a result of the Li polyhedra connecting the $[PO_xS_{4-x}]^{3-}$ tetrahedra. The Li polyhedra seem to be much less defined, indicated by the rapid decrease in oscillation intensity, but the physical limits for Li–S, and Li–O bond lengths force the $[PO_xS_{4-x}]^{3-}$ tetrahedron to keep a certain distance from each other. The orientation of $[PO_xS_{4-x}]^{3-}$ tetrahedra towards each other could still be random, indicated by the lack of distinct features on top of the oscillations. The correlation length, the maximum distance to which some order can be observed, decreases with increasing oxygen content from *ca.* 20 for the pure thiophosphate to about 17 Å for the sample with 30% P–O fraction. The decreasing correlation length with increasing oxygen content can be explained by an added

uncertainty for the occurring bond lengths in the material with higher oxygen substitution since P–O and Li–O bonds should be shorter than P–S and Li–S bonds. The overall low correlation length of all samples reveals the glassy nature of the materials without any long-range order. Compared to LIO samples, the PDFs of the LIPSO samples exhibit more and sharper peaks extending to higher distances (see Fig. 3(a)). The low r region is again dominated by intra $[PS_4]^{3-}$ peaks of the thiophosphate phase. The peaks in the mid and high r region starting from around 8 Å do not belong to a thiophosphate phase, instead, they can be fitted with β-Li_3PO_4 (Fig. S8†). The red dashed line in Fig. 3(a) marks the transition from LPS to LPO signals. The peak intensities for $r < 8$ Å increase as the oxygen content increases. The correlation length of the phosphate phase also appears to increase; however, this information is superimposed by the residual crystalline LPO causing an overall increase in peak intensity. The correlation length in the thiophosphate phase can be assumed to have a similar range as in the LIO series. The nanocrystalline β-Li_3PO_4 phase can be fitted individually. That way we can subtract all contributions from the LPO phase to the total PDF and the difference curve resulting from the fit then represents the pure amorphous thiophosphate phase. This amorphous PDF can be compared to the samples from the LIO series to investigate possible differences in the amorphous phase caused by the synthesis route. However, as seen in the example of samples with 30% oxygen content in Fig. 3(d and e), the LIO sample PDF (dotted brown line) lies perfectly on top of the difference curve (green line). The total LIPSO sample PDF (black line) and the fit for the LPO phase (red line) are also shown. From Rietveld-like fitting (PDFgui), the crystallite size of the β-Li_3PO_4 particles was calculated and the same trend as described for the Rietveld refinements was found. This indicates an overall decrease of the X-ray coherent domain size with increasing oxygen content, in this case from *ca.* 14 nm for the sample with 10% LPO to 10.6 nm for the sample with 40% LPO. Consequently, the LIPSO samples must be composed of β-Li_3PO_4 nanocrystals inside an amorphous matrix, built mainly from $[PS_4]^{3-}$ tetrahedra.

PDF analysis yielded a first understanding of the glass structure and composition. However, we were not able to clearly identify all polyhedral units. At the same time, the oxygen correlations in the local structure were not visible due to the low scattering cross-section of oxygen for X-rays. Therefore, additional spectroscopic methods were applied to examine the glass-forming structural units.

Raman spectroscopy was performed on all starting materials and oxy-sulfide mixtures to investigate the bonding situation. The results can be viewed in Fig. 4(a and b). Fig. S4(b)† displays the characteristic Raman spectra of the starting materials Li_2S and P_2S_5 and glass Li_3PS_4. The Raman bands of P_2S_5 and Li_2S were not observed in glass Li_3PS_4 after ball milling and all main bands of glass Li_3PS_4 can be attributed to the internal vibration of the $[PS_4]^{3-}$ anion with T_d symmetry.[57,58] Fig. 4(a) displays the Raman spectra of the LIPSO series including the starting materials Li_3PS_4 and

Li_3PO_4. The spectra show a high degree of similarity for all oxygen concentrations. The main peak at 421 cm^{-1} can be assigned to the symmetric P–S stretching band of the $[PS_4]^{3-}$ tetrahedron. The bands at 190, 265, and 562 cm^{-1} also belong to the same structural unit and can be attributable to the ν_2 symmetric, ν_4 asymmetric S–P–S bending vibrations, and ν_3 antisymmetric P–S stretching vibration. The small shoulder band at around 370 cm^{-1} is assigned to the units of $[P_2S_6]^{4-}$.[59,60] This minor impurity is commonly found in ball-milled Li-thiophosphate (LPS) probably due to the inhomogeneous reaction during the milling.[61] Another tiny band at around 490 cm^{-1} arises from polysulfide chain ions, which may be the offset of $[P_2S_6]^{4-}$ to $[PS_4]^{3-}$.[62,63] As expected, $[PS_4]^{3-}$ ions are the dominant species.[55] In comparison to crystalline LPS, the oxy-sulfide glasses show peak broadening and a slight shift to higher frequencies. Additionally, two more bands can be observed around 942 cm^{-1}. The sharp band at lower wavenumbers can be assigned to the symmetrical stretching vibration of the P–O bonds ν_1 in $[PO_4]^{3-}$ from the crystalline β-Li_3PO_4. The peak shoulder with a slightly higher wavenumber can also be assigned to the symmetrical stretching vibration ν_1 $[PO_4]^{3-}$ units but from the milled amorphous Li_3PO_4. The peak broadening can be explained by the amorphous nature of the glasses, while the shift could be a result of strain introduced by the harsh ball milling procedure.

The Raman spectra of the LIO series, presented in Fig. 4(b), feature the same bands as found in the LIPSO spectra except for the small bands around 942 cm^{-1} that were attributed to $[PO_4]^{3-}$ units. The absence of the $[PO_4]^{3-}$ vibration signal confirms that no crystalline Li_3PO_4 formed during the synthesis. The presence of amorphous Li_3PO_4 cannot be excluded, judging from this measurement, but the amount of $[PO_4]^{3-}$ units is small compared to the LIPSO samples. Other $[PO_xS_{4-x}]^{3-}$ units do not contribute to the Raman signal because the tetrahedral symmetry is broken, changing the selection rules for the relevant energy transitions.

^{31}P MAS NMR measurements are displayed in Fig. 4(c and d). All spectra are dominated by a broad peak at 83.1 ppm which was assigned to the overlap of $[PS_4]^{3-}$ and $[PS_3O]^{3-}$ resonances. The shift of this peak compared to the crystalline LPS, and the broadening of the line shape, reflects the glass-ceramic property (crystalline LPO phase in a glassy matrix) of the oxysulfide mixtures $(1 - x)Li_3PS_4–xLi_3PO_4$.[64] Two additional broad resonances at around 69.5 ppm and 36.3 ppm in the spectra for the milled mixtures are attributed to $[PS_2O_2]^{3-}$ and $[PSO_3]^{3-}$ units, respectively.[65] The other two broad resonances at a low chemical shift of 8.8 ppm and −2.8 ppm can probably be attributed to the poorly crystalline orthophosphate tetrahedron $[PO_4]^{3-}$ and dimeric $[P_2O_7]^{4-}$ units after ball milling, respectively.[66–69] The sharp peak of crystalline $[PO_4]^{3-}$ at 10.9 ppm still exists in the oxysulfide mixtures of the LIPSO samples agreeing with the previous results. The presence of the additional units $[PS_3O]^{3-}$, $[PS_2O_2]^{3-}$, $[PSO_3]^{3-}$, and dimeric $[P_2O_7]^{4-}$ units reveal that the sulfur atoms in $[PS_4]^{3-}$ tetrahedron are partially substituted by the oxygen atoms from $[PO_4]^{3-}$ tetrahedron. The main difference
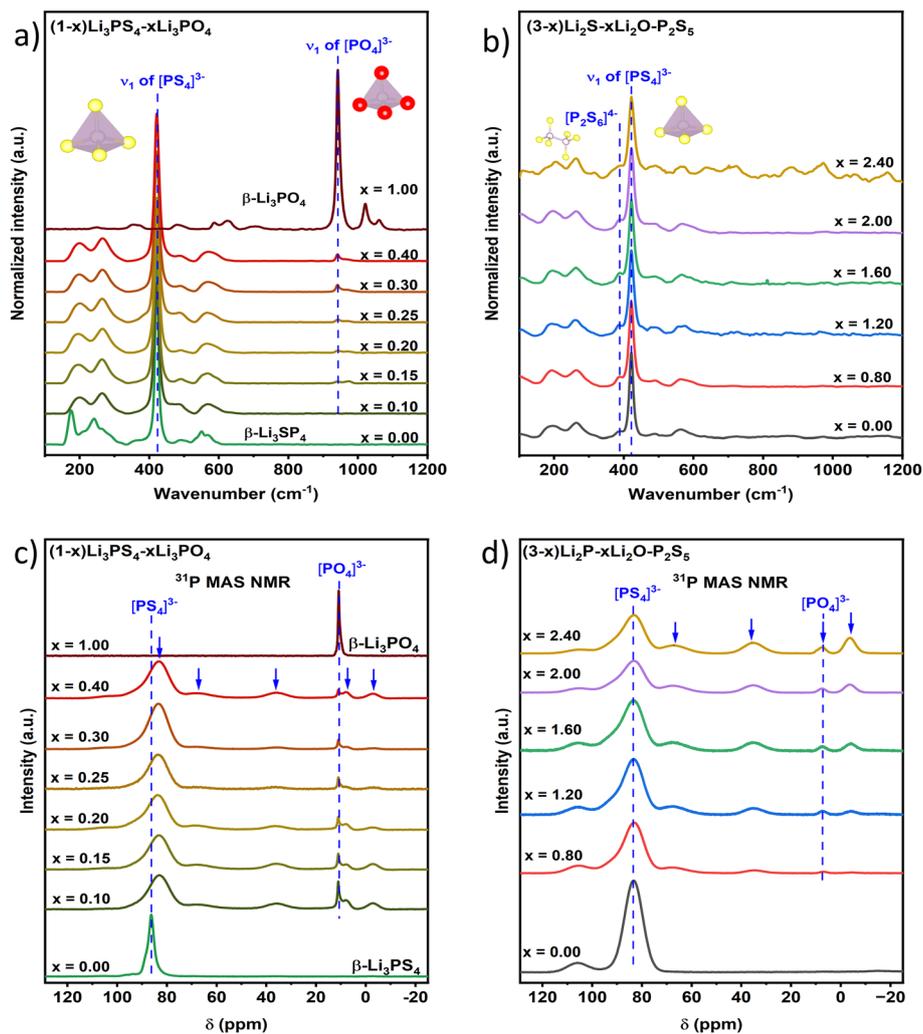
Fig. 4 (a and b) Raman spectra of LIPSO (a) and LIO (b) series with assignment of the main bands and sketches of PS_4^{3-}, PO_4^{3-}, and $P_2S_6^{4-}$ structural units. (c and d) ^{31}P MAS NMR spectra of LIPSO (c) and LIO (d), blue arrows pointing to the peaks of mixed $[PO_xS_{4-x}]^{3-}$ (a and c taken from Luo 2022).[53]

between LIPSO and LIO is again the persistence of a sharp signal corresponding to β-Li_3PO_4 nanocrystals for the LIPSO samples. However, these ^{31}P MAS NMR results demonstrate that in both experimental series, sulfur was partially replaced by oxygen and as a result, mixed $[PO_xS_{4-x}]^{3-}$ units were formed. The intensities of the mixed tetrahedron scale with the oxygen content for LIO. For the LIPSO series, though, there is no clear trend visible. In both cases signals for all possible substitutions, $[PO_xS_{4-x}]^{3-}$ with $0 \leq x \leq 4$, can be found in all samples, indicating that the ball milling procedure offers little control over the oxygen distribution in the produced material.

After a careful structural analysis of the oxy-sulfide glasses, we know which structural units are present in each glass and to what degree they are ordered. The materials yielded from LIPSO and LIO have shown significant structural deviations. While LIO samples can be categorized as glasses, we found residual β-Li_3PO_4 nanocrystals embedded in the amorphous thiophosphate matrix in all LIPSO samples, resulting from the

higher chemical and mechanical stability of Li_3PO_4 compared to Li_3PS_4. These crystallites lead us to label the LIPSO samples as glass-ceramics. Therefore, we expect different physical and chemical properties from the two sets of materials, although the overall stoichiometry is identical. The amorphous matrix, which makes up most of the material for all samples, primarily consists of $[PS_4]^{3-}$ tetrahedra and varying amounts of mixed $[PO_xS_{4-x}]^{3-}$ species. For LIPSO some additional units like $[P_2S_6]^{4-}$ and $[P_2S_7]^{4-}$ were also found. These units are quantitatively more common in the LIO series. The reason for that is most likely that the Li_3PS_4 glass was calcinated to form β-Li_3PS_4 before mixing with β-Li_3PO_4 in LIPSO, whereas Li_3PS_4 glass was formed *in situ* during synthesis in the LIO series. The calcination process has been reported to alter the amount of impurities.[34,60]

In summary, both synthesis routes yielded materials with the same stoichiometry and structural units. The main difference lies in the relative quantity of these structural units and

the oxygen distribution. Li_3PO_4 is both physically and chemically too stable to fully react under the given ball milling conditions, therefore some phosphate crystallites remain in the products of the LIPSO series. The mix of crystalline particles and amorphous matrix classifies these materials as glass ceramics. In contrast, products from the LIO series are more homogeneous and can be classified as glasses.

Electrochemical analysis

Different conductivity values have been published for oxy-sulfide glasses and glass ceramics.[17,19,21,22,24] Fig. 5 depicts the electrochemical impedance spectroscopy (EIS) measurements of the LIPSO and LIO series. To examine the influence of crystalline Li_3PO_4 particles inside the amorphous Li_3PS_4 glass, a third material series was prepared by 15 min mechanical mixing of β-Li_3PO_4 with amorphous Li_3PS_4 in a mortar.

Exemplary Nyquist plots of the LIO1, 3 and 5 samples measured at various temperatures and with two different measurements, cells are presented in Fig. S10.† Multiple pellets from each sample were measured in a custom-made cell (Fig. S1†) and an additional pellet was measured in a CompreDrive set-up (rhd instruments GmbH & Co. KG, Germany). The conductivity values were extracted by using the circle fit function of the program EC-lab to calculate the semicircle diameter. In the CompreDrive set-up, some inductive coupling within the set-up prevented the resolution of semicircles in the Nyquist plots, thus the conductivity was calculated from the x-axis intersection. The CompreDrive measurements yielded systematically higher conductivity values, which can be explained by the more accurate pressure control. The conductivity trend was identical with both measurement setups. The error bars depicted in Fig. 5 represent the standard deviation when all measurements from both setups are considered.
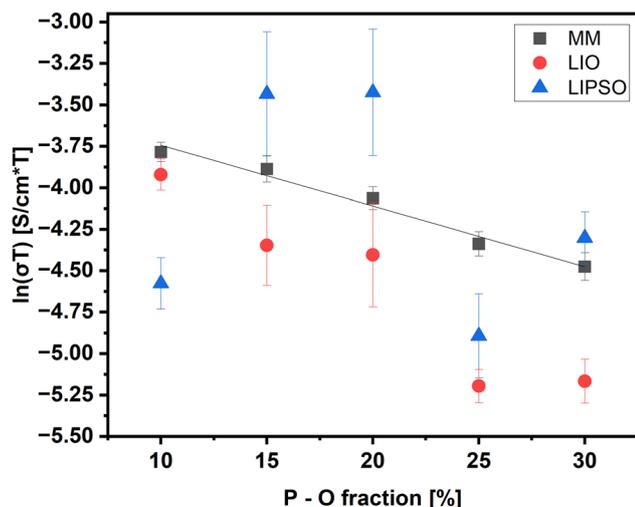
In order to rule out any systematic influences from the macrostructure of the pellets on the conductivity measurement, the porosity of the measured pellets was evaluated by calculating their relative density. The relative density is defined as the ratio of the geometric density of the pellet and the real density of the material. Density measurements were conducted on three samples (LIOref, LIO2 and LIO4; 0, 15 and 25% oxygen substitution) using a He-gas pyknometer to get a fair estimate of the real density values and account for changes with increasing oxygen substitution. The three remaining values for the samples with 10, 20 and 30% oxygen substitution were estimated from the measured values. The real-density values used for the calculation were; 1.905, 1.914, 1.909, 1.904, and 1.899 for samples with 10, 15, 20, 25 and 30% oxygen substitution respectively. Using the above values, all calculated relative densities of the measured pellets were in the range of 86 to 89% with no clear correlation to the oxygen substitution level.

As seen in the plot in Fig. 5, the three series do not follow the same conductivity trends. The mechanical mix, from here on referred to as MM, has a linear behaviour on the logarithmic scale as expected for a mixture of a highly conducting with a poorly conducting material. The trend for the LIO series is similar in the sense that the Li-ion conductivity decreases with increasing oxygen content. However, the decrease in conductivity is stronger, and the data points scatter more, showing a nonlinear behaviour. Surprisingly, the LIPSO series exhibits a very different trend with a low conductivity at 10% P–O bonds, then a maximum at 15–20% followed by a dip to 25% and again a slight increase at 30% P–O bonds.

To understand this unusual behaviour, we need to take a closer look at the structural data. As mentioned earlier, the main difference between the LIPSO and LIO glasses is the presence of β-Li_3PO_4 nanocrystals in LIPSO samples and the oxygen distribution, which is related to the relative quantity of various structural units. The MM series strongly suggests that the β-Li_3PO_4 crystals found in the LIPSO series are not responsible for the differing conductivity trend, since an increasing amount of crystalline β-Li_3PO_4 should, on the logarithmic scale, lead to a linear decrease in the ion conductivity. Therefore, we used the ^{31}P MAS NMR spectra to determine the relative quantity of the reacted $[PO_xS_{4-x}]^{3-}$ tetrahedra.

The NMR spectra were deconvoluted and fitted with Gaussian/Lorentzian lines using dmfit.[70] The results of the analyses are summarised in Table S1† and visually displayed in Fig. 6(a and b). Fig. 6(c) depicts a statistical distribution of the different tetrahedra given the respective oxygen content. As expected, the real distribution in the samples differs from a purely statistical distribution. The $[PO_4]^{3-}$ concentration is too high in all samples, the $[PO_3S]^{3-}$ and $[PO_2S_2]^{3-}$ concentrations are higher than in the statistical distribution for low oxygen content and lower for high oxygen content. The results suggest a tendency for oxygen to cluster together and build highly substituted species.

In the LIO series, the amount of oxygen-substituted tetrahedra increases almost linearly with increasing oxygen content.
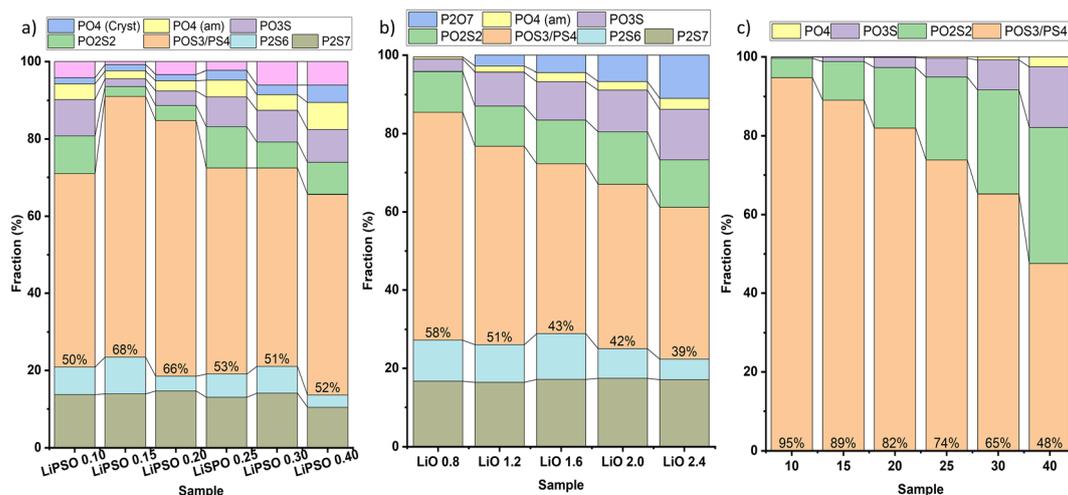

Fig. 5 Logarithm of room temperature conductivity values, derived from EIS measurements, plotted against the total P–O fraction for LIPSO, LIO, and mechanical mix (MM) synthesis procedures.

Fig. 6 Quantities of structural units in LIPSO (a) and LIO (b) compared with statistical distribution (c).

The amount of $[P_2S_7]^{4-}$ impurities stays almost constant over the whole concentration range, while the $[P_2S_6]^{4-}$ amount seems to decrease for higher oxygen contents. The LIPSO series shows a non-linear change of the different structural units, only the $[P_2S_7]^{4-}$ content is again almost constant.

The peak integrals show a clear correlation between the quantities of the highly substituted tetrahedra (2 or more oxygen atoms on one tetrahedron) and the ionic conductivity. Fig. 7(a and b) illustrate the sum of all oxygen-containing species with $n_O > 2$ (black dots) and the corresponding ion conductivity of all samples for LIPSO and LIO (red dots). Both graphs mirror each other, showing an inverse correlation. A high amount of oxygen clustering leads to low conductivity and *vice versa*. The same correlation can also be observed by just plotting the amount of amorphous $[PO_4]^{3-}$ units and the conductivity (see Fig. 7(c and d)). While the correlation is clearly visible, the mirroring is not perfect for all the displayed graphs. When looking at the $[PO_4]^{3-}$ content, this can be explained by the overall low quantity of $[PO_4]^{3-}$ units in the materials compared to other structural units that also affect the ion conductivity. The amount of $[PO_4]^{3-}$ is generally higher in the LIPSO series, whereas there are more $[P_2S_6]^{4-}$ and $[P_2S_7]^{4-}$ impurities found in the LIO samples. All the different structural units and their distribution within the materials contribute to the total ion conductivity, which may explain why some features in the conductivity trend are not perfectly represented in the structural unit fraction curves. The inverse correlation of ionic conductivity and the fraction of highly substituted tetrahedra becomes evident when plotting the conductivity values against the combined fraction of PO_4, PO_3S, and PO_2S_2, which shows an almost linear trend across both experimental series (Fig. 7(e)). The same plot with only the amorphous PO_4 fraction on the *x*-axis yields two separate correlations, one for each experimental series. The correlations are qualitatively similar, showing the decrease in conductivity for increasing amounts of PO_4 units (Fig. 7(f)), but they are offset

on the *x*-axis. The LiPSO samples generally contain more PO_4 units and display similar conductivity values as the LIO samples for higher PO_4 fractions. The reason for this offset is most likely the higher amount of PO_3S, and PO_2S_2 units in the LIO samples, which leads to a reduced conductivity even though the PO_4 fraction is comparatively low. The scattering of the data points reveals that there must be other factors influencing the Li-ion conductivity.

The influence of oxygen distribution in oxy-sulfides was theoretically predicted for crystalline β-LPS by Banerjee *et al.*[71] Their study found a higher theoretical ion conductivity when oxygen atoms were homogeneously dispersed than for the case where they were clustered together for two different oxygen concentrations. These calculations even predicted an increase in ion conductivity for small amounts of dispersed oxygen. The $[PO_4]^{3-}$ units have the highest density of oxygen atoms and therefore seem to be most detrimental to the Li-ion conductivity. Our experimental findings therefore agree well with the calculations.

It should be noted, that a repetition of the experiments could only qualitatively reproduce the displayed conductivity trends. For the LIO series, the control experiment yielded a more linear, but otherwise comparable conductivity trend where the conductivity continuously decreases with increasing oxygen content. For the LIPSO series, another nonlinear zigzag trend was discovered, which did not agree with the previous one, exhibited in Fig. 5. However, following the same quantitative analysis of structural units leads to the same results, that different *O*-substituted polyhedra have varying influence on the Li-ion conductivity and highly substituted species are most detrimental (see Fig. S11†). Therefore, the statements of this study could be verified. The dissimilar conductivity trends, when only comparing the chemical composition, suggest a reproducibility problem with the ball-milling procedure. The lack of control over the processes inside the milling jar due to the statistical nature of collisions and energy
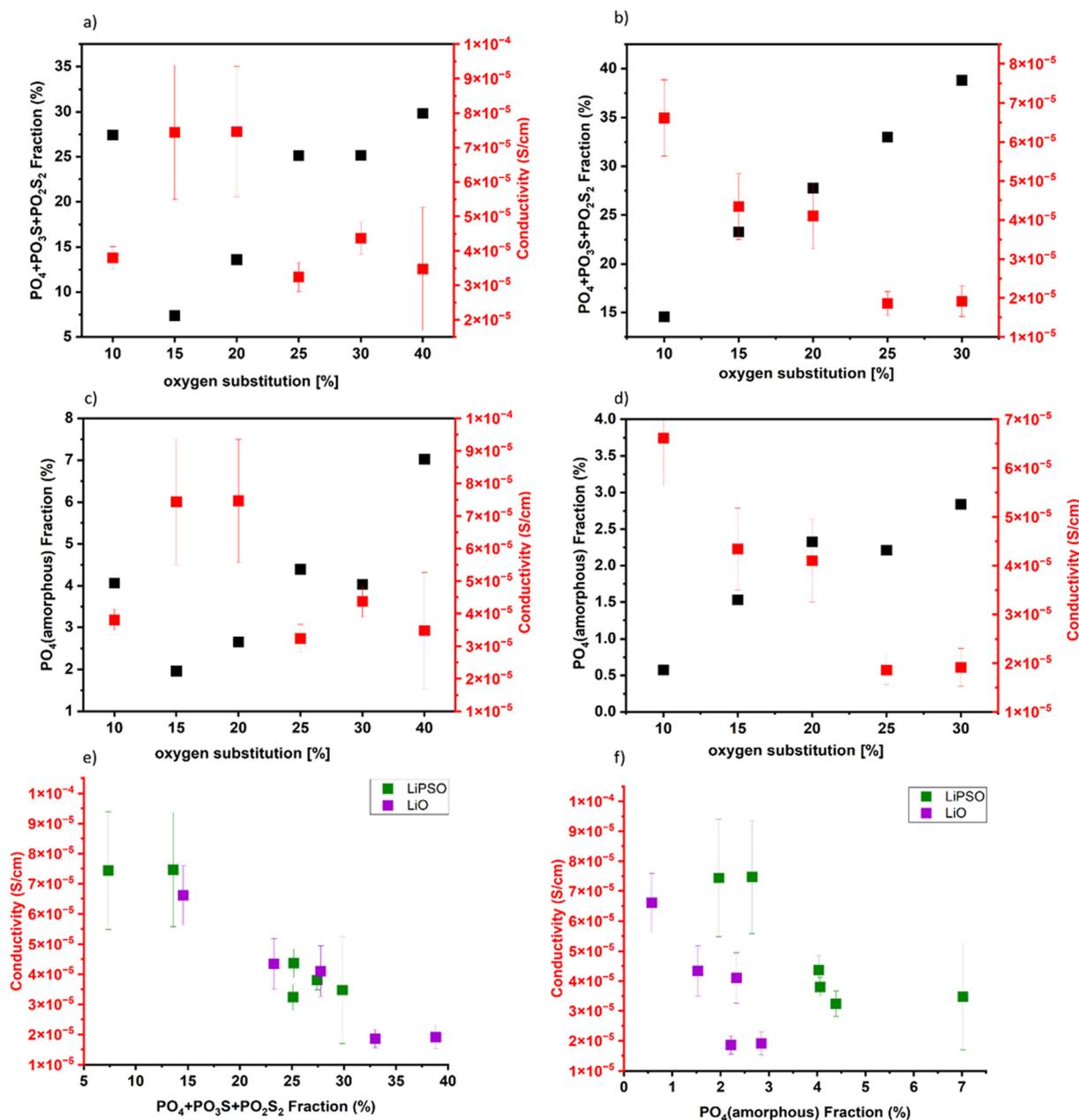
Fig. 7 (a and b) combined fraction of all tetrahedra with $n_O > 2$ (black) and corresponding Li-ion conductivity (red) vs. total oxygen substitution of LIPSO (a) and LiO (b). (c and d) Amorphous PO_4 fraction and Li-ion conductivity vs. total oxygen substitution of LIPSO (c) and LIO (d). (e and f) Li-ion conductivity vs. fraction of all tetrahedra with $n_O > 2$ (e) and amorphous PO_4 fraction (f) across all samples from both LIPSO (green) and LiO (purple) samples.

transfer leads to somewhat random results. As these processes are irreversible, changes in the configuration can accumulate over time rather than averaging out. The reproducibility problem seems to be more pronounced the less likely the desired reaction is. The Li_3PO_4 precursor used for the LIPSO series is the most stable compound in the system and requires optimal conditions and high energy input to react with Li_3PS_4. Hence, some phosphate particles remain unreacted. Suitable conditions are therefore not as frequently met during the milling process and small variations in the mixing of the pre-

cursors or the powder distribution within the milling jar, over a long milling time, cause significant discrepancies in the total number of reaction events. On the other hand, the LIO route seems to be less sensitive because the reactants are more reactive. Hence, there are multiple pathways leading to the same result.

Calculations

In order to further investigate the influence of oxygen on Li diffusivity, we additionally performed molecular dynamics

simulations. To this end, different glass models with 0%, 5%, 10%, 15%, 20% and 25% overall oxygen content were generated. At every composition, the oxygen was distributed in different ways, such that only one type of the oxygen-containing units PS_3O, PS_2O_2, PSO_3, or PO_4 is present. All the remaining units in the models were kept at PS_4. Visual representations of simulated glasses with 20% P–O fraction and the four different oxygen distributions are displayed in Fig. 8(a–d). The defined oxygen distribution within the simulated glasses allows us to separately study the effects of the overall oxygen content and the different tetrahedron types. All structures contained 2048 atoms and were simulated with molecular dynamics for several nanoseconds at 500 K. We note that such simulated model sizes are approximately 10 times larger and that the corresponding timescales are approximately 10–100 longer than what is typically accessible with *ab initio* molecular dynamics simulations, commonly used to study diffusion in solid electrolytes. This enables us to study the properties of the material at comparably low temperatures without reverting to extrapolations from high temperatures, while still retaining good statistics for the Li diffusion. Our simulations are realized by employing an atomic cluster expansion (ACE) potential, trained from density functional theory (DFT) data for this purpose.

The obtained tracer diffusion coefficients are shown in Fig. S12† and have been used to compute conductivity σ *via* the Nernst–Einstein equation. The calculated Li-ion conductivities are plotted against the P–O fraction in Fig. 8(f). We find an obvious trend: an increasing overall oxygen content leads to decreasing conductivity, independent of the combination of the tetrahedra types. Qualitatively, this trend is similar to the results of the LIO route. Moreover, there are no indications that the conductivity increases at small oxygen contents, as seen for the LIPSO route. One reason for this discrepancy could be the much more complex local structure and microstructure, (*e.g.*, mixtures of all tetrahedra types, crystalline remnants of Li_3PO_4, non-tetrahedral structure units like P_2S_7, P_2S_6, or P_2O_7) that are observed in the experiments.

The second observation is the dependence of the conductivity as a function of the structure units at the same overall oxygen content: in general, we find that oxygen-rich structural units (PO_4, PSO_3) lead to a stronger decrease of the conductivity than the oxygen-poor structural units (PS_2O_2, PS_3O). This is mostly in line with the conclusion drawn from the experimental results as discussed above. Surprisingly, however, we do not find a combination of PS_2O_2 units to be detrimental to the conductivity, as has been shown by simulations of Banerjee *et al.*[71] for oxygen substitution in crystalline Li_3PS_4. Unfortunately, there is no information on how the even more oxygen-rich units affect the transport properties. Nevertheless, this could indicate that the interactions between different oxygen-containing tetrahedral units and Li ions is much different in glasses than in the crystalline counterpart. As a matter of fact, our glasses containing $PS_4 + PS_2O_2$ units even outperform glasses with $PS_4 + PS_3O$ units at several oxygen contents. One reason for this could be that we only tested one
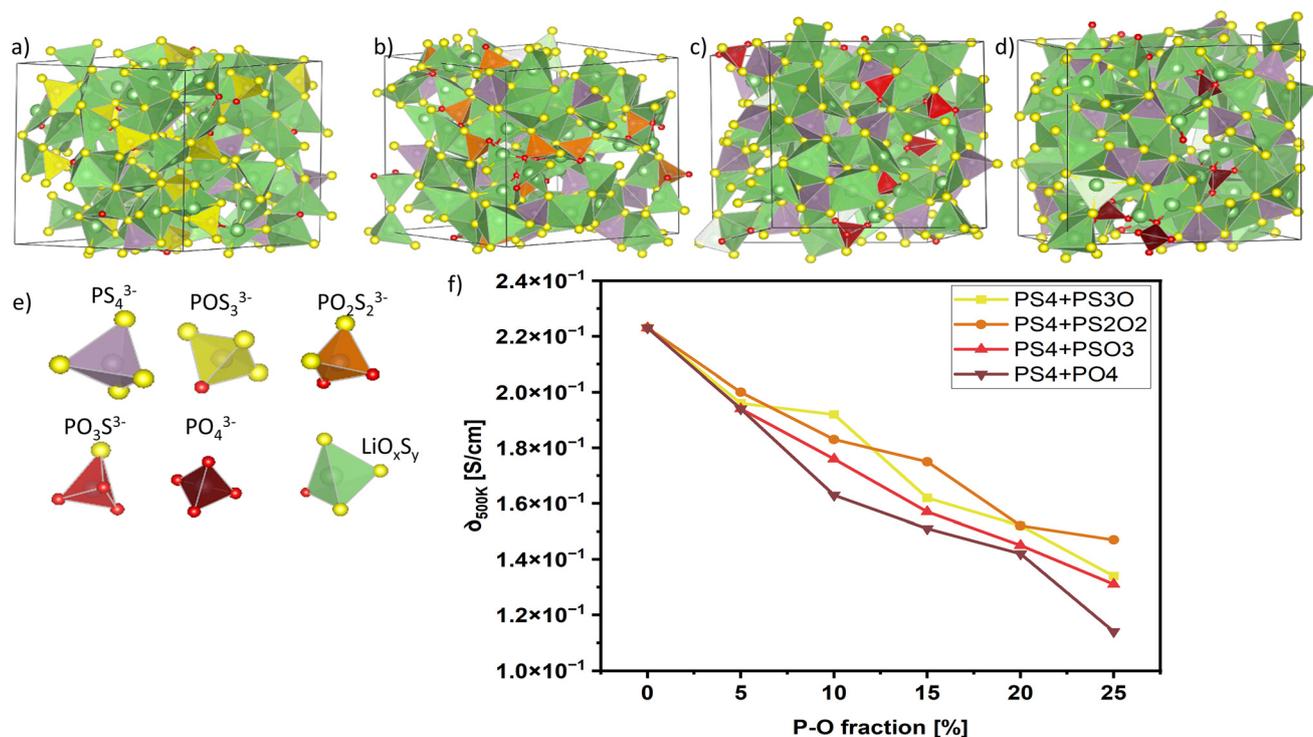

Fig. 8 (a–d) Simulated structures with only PS_4 and POS_3 (a), PO_2S_2 (b), PO_3S (c), PO_4 (d) units at 20% P–O fraction. (e) Description of the different polyhedra. (f) Calculated Li-ion conductivities against P–O fraction for the displayed structures.

way of randomly distributing the oxygen-containing tetrahedron in our models, and a different distribution (*e.g.*, more homogeneous or more clustered arrangements) might behave differently. Such an analysis, potentially also including temperature effects and extrapolating to 300 K, however, goes beyond the scope of this study and needs to be covered elsewhere.

Conclusions

This study shows the importance of careful experiment planning and material characterization and may guide future material development. Our findings may also explain the large spread of conductivity values found in the literature for these kinds of oxy-sulfide glasses and glass ceramics, as often only the total oxygen concentration is considered, while the oxygen distribution and exact structural units are neglected. We could show that the stoichiometry alone is not a sufficient description for the Li oxysulfides. The choice of precursor materials and synthesis conditions offer possibilities to further tune the properties of materials within the same chemical composition. The results also may be transferrable to other amorphous or semi-crystalline systems, where a lack of reducible symmetry makes the investigation of structural units a valuable part of material characterization.

Further investigations will focus on the development of a more realistic structure model, including information on the Li environment. Such a model could help investigate the effects of oxygen distribution on a larger length scale, *e.g.* clustering of oxygen-containing units. Moreover, models are needed to gain a better understanding of the conduction mechanism inside the amorphous matrix.

Data availability

Data for this article, including XRD, PDF, NMR, Raman and EIS data are available at Zenodo "Influence of oxygen distribution on the Li-ion conductivity in oxy-sulfide glasses – taking a closer look" at **https://zenodo.org/deposit/11197809**.

Author contributions

Ramon Zimmermanns: project administration, investigation, formal analysis, conceptualisation, validation and visualisation for all data related to the LIO series as well as analysis of PDF data. Writing – original draft. Xianlin Luo: investigation, formal analysis, conceptualisation, validation and visualisation for the LIPSO series. Writing – original draft. Anna-Lena Hansen: conceptualisation, project administration, supervision, acquisition of PDF data. Review and editing. Marcel Sadowski: investigation, formal analysis, validation and visualisation of all simulation related data. Writing – original draft. Qiang Fu: investigation LIPSO series, review and editing. Karsten Albe: supervision for the computational part. Review

and editing. Sylvio Indris: supervision LIPSO, review and editing. Michael Knapp: supervision LIO, funding acquisition. Review and editing. Helmut Ehrenberg: resources for the experimental part. Review and editing.

Conflicts of interest

There are no conflicts to declare.

Acknowledgements

References

1 J. B. Goodenough and K.-S. Park, The Li-ion rechargeable battery: a perspective, *J. Am. Chem. Soc.*, 2013, **135**(4), 1167–1176, DOI: **10.1021/ja3091438**, PMID: 23294028.

2 G. Jeong, Y.-U. Kim, H. Kim, Y.-J. Kim and H.-J. Sohn, Prospective materials and applications for Li secondary batteries, *Energy Environ. Sci.*, 2011, **4**(6), 1986, DOI: **10.1039/c0ee00831a**.

3 T.-H. Kim, J.-S. Park, S. K. Chang, S. Choi, J. H. Ryu and H.-K. Song, The Current Move of Lithium Ion Batteries Towards the Next Phase, *Adv. Energy Mater.*, 2012, **2**(7), 860–872, DOI: **10.1002/aenm.201200028.**

4 M. Li, J. Lu, Z. Chen and K. Amine, 30 Years of Lithium-Ion Batteries, *Adv. Mater.*, 2018, e1800561, DOI: **10.1002/adma.201800561**, PMID: 29904941.

5 G. Zubi, R. Dufo-López, M. Carvalho and G. Pasaoglu, The lithium-ion battery: State of the art and future perspectives, *Renewable Sustainable Energy Rev.*, 2018, **89**(3), 292–308, DOI: **10.1016/j.rser.2018.03.002**.

6 H. Kawamura, M. LaFleur, K. Iversen and H. W. J. Cheng, *Lithium-Ion Batteries: A Pillar for a Fossil Fuel-Free Economy?*,

United Nations Department of Economic and Social Affairs, 2021.

7 T. M. Bandhauer, S. Garimella and T. F. Fuller, A Critical Review of Thermal Issues in Lithium-Ion Batteries, *J. Electrochem. Soc.*, 2011, **158**(3), R1, DOI: **10.1149/1.3515880**.

8 A. Mauger and C. M. Julien, Critical review on lithium-ion batteries: are they safe? Sustainable?, *Ionics*, 2017, **23**(8), 1933–1947, DOI: **10.1007/s11581-017-2177-8**.

9 A. Manthiram, X. Yu and S. Wang, Lithium battery chemistries enabled by solid-state electrolytes, *Nat. Rev. Mater.*, 2017, **2**(4), 16103, DOI: **10.1038/natrevmats.2016.103**.

10 F. Zheng, M. Kotobuki, S. Song, M. O. Lai and L. Lu, Review on solid electrolytes for all-solid-state lithium-ion batteries, *J. Power Sources*, 2018, **389**(5), 198–213, DOI: **10.1016/j.jpowsour.2018.04.022**.

11 A. Kraytsberg and Y. Ein-Eli, Recent Developments in the Field of Sulfide Ceramic Solid-State Electrolytes, *Energy Technol.*, 2023, **11**(6), 2201291, DOI: **10.1002/ente.202201291**.

12 F. Mizuno, A. Hayashi, K. Tadanaga and M. Tatsumisago, High lithium ion conducting glass-ceramics in the system $Li_2S–P_2S_5$, *Solid State Ionics*, 2006, **177**(26–32), 2721–2725, DOI: **10.1016/j.ssi.2006.04.017**.

13 M. Tatsumisago, S. Hama, A. Hayashi, H. Morimoto and T. Minami, New lithium ion conducting glass-ceramics prepared from mechanochemical $Li_2S–P_2S_5$ glasses, *Solid State Ionics*, 2002, **154–155**, 635–640, DOI: **10.1016/S0167-2738(02)00509-X**.

14 Y. Kato, S. Hori, T. Saito, *et al.*, High-power all-solid-state batteries using sulfide superionic conductors, *Nat. Energy*, 2016, **1**(4), 652, DOI: **10.1038/NENERGY.2016.30**.

15 K. Wissel, L. M. Riegger and C. Schneider, *et al.*, Dissolution and Recrystallization Behavior of Li_3PS_4 in Different Organic Solvents, *arXiv*, 2022, DOI: **10.48550/arXiv.2209.13955**, preprint.

16 K. Wissel, L. M. Riegger, C. Schneider, *et al.*, Dissolution and Recrystallization Behavior of Li_3PS_4 in Different Organic Solvents with a Focus on N-Methylformamide, *ACS Appl. Energy Mater.*, 2023, **6**(15), 7790–7802, DOI: **10.1021/acsaem.2c03278**.

17 A. Hayashi, K. Tadanaga, M. Tatsumisago, T. Minami and Y. Miura, Structural Change Accompanying Crystallization in the Lithium Ion Conductive Li_2S-SiS_2-Li_3PO_4 Oxysulfide Glasses, *J. Ceram. Soc. Jpn.*, 1999, **107**(1246), 510–516, DOI: **10.2109/jcersj.107.510**.

18 K. Minami, F. Mizuno, A. Hayashi and M. Tatsumisago, Structure and properties of the $70Li_2S·(30−x)P_2S_5·xP_2O_5$ oxysulfide glasses and glass–ceramics, *J. Non-Cryst. Solids*, 2008, **354**(2–9), 370–373, DOI: **10.1016/j.jnoncrysol.2007.07.059**.

19 A. Neveu, V. Pelé, C. Jordy and V. Pralong, Exploration of Li–P–S–O composition for solid-state electrolyte materials discovery, *J. Power Sources*, 2020, **467**, 228250, DOI: **10.1016/j.jpowsour.2020.228250**.

20 N. Machida, Y. Yoneda and T. Shigematsu, Mechanochemical Synthesis of Lithium Ion Conducting Materials in the System $Li_2O–Li_2S–P_2S_5$, *J. Jpn. Soc. Powder Powder Metall.*, 2003, **51**(2), 91–97.

21 J. E. Trevey, J. R. Gilsdorf, S. W. Miller and S.-H. Lee, Li_2S–$Li_2O–P_2S_5$ solid electrolyte for all-solid-state lithium batteries, *Solid State Ionics*, 2012, **214**, 25–30, DOI: **10.1016/j.ssi.2012.02.034**.

22 H. Tsukasaki, H. Morimoto and S. Mori, Ionic conductivity and thermal stability of $Li_2O–Li_2S–P_2S_5$ oxysulfide glass, *Solid State Ionics*, 2020, **347**(6), 115267, DOI: **10.1016/j.ssi.2020.115267**.

23 N. H. H. Phuc, T. Maeda, T. Yamamoto, H. Muto and A. Matsuda, Preparation of Li_3PS_4–Li_3PO_4 Solid Electrolytes by Liquid-Phase Shaking for All-Solid-State Batteries, *Electron. Mater.*, 2021, **2**(1), 39–48, DOI: **10.3390/electronicmat2010004**.

24 K. Takada, M. Osada, N. Ohta, *et al.*, Lithium ion conductive oxysulfide, Li_3PO_4–Li_3PS_4, *Solid State Ionics*, 2005, **176**(31–34), 2355–2359, DOI: **10.1016/j.ssi.2005.03.023**.

25 B. Huang, X. Yao, Z. Huang, Y. Guan, Y. Jin and X. Xu, Li_3PO_4-doped $Li_7P_3S_{11}$ glass-ceramic electrolytes with enhanced lithium ion conductivities and application in all-solid-state batteries, *J. Power Sources*, 2015, **284**, 206–211, DOI: **10.1016/j.jpowsour.2015.02.160**.

26 S. W. Martin, Glass and Glass-Ceramic Sulfide and Oxy-Sulfide Solid Electrolytes, in *Handbook of Solid State Batteries and Capacitors*, ed. N. J. Dudney, W. C. West and J. Nanda, World Scientific Publishing Co. Pte Ltd, 2nd edn, 2015, pp. 433–501.

27 Ö. U. Kudu, T. Famprikis, B. Fleutot, *et al.*, A review of structural properties and synthesis methods of solid electrolyte materials in the Li_2S – P_2S_5 binary system, *J. Power Sources*, 2018, **407**(4), 31–43, DOI: **10.1016/j.jpowsour.2018.10.037**.

28 S. Mo, P. Lu, F. Ding, *et al.*, High-temperature performance of all-solid-state battery assembled with $95(0.7Li_2S-0.3P_2S_5)$-$5Li_3PO_4$ glass electrolyte, *Solid State Ionics*, 2016, **296**, 37–41, DOI: **10.1016/j.ssi.2016.09.002**.

29 K. Kaup, L. Zhou, A. Huq and L. F. Nazar, Impact of the Li substructure on the diffusion pathways in alpha and beta Li_3PS_4: an in situ high temperature neutron diffraction study, *J. Mater. Chem. A*, 2020, **8**(25), 12446–12456, DOI: **10.1039/d0ta02805c**.

30 H. Yamada, K. Ohara, S. Hiroi, *et al.*, Lithium Ion Transport Environment by Molecular Vibrations in Ion-Conducting Glasses, *Energy Environ. Mater.*, 2024, **7**(3), e12612, DOI: **10.1002/eem2.12612**.

31 M. Yoshimoto, T. Kimura, A. Sakuda, *et al.*, Crystallization process of Li_3PS_4 investigated by X-ray total scattering measurement and the reverse Monte Carlo method, *Solid State Ionics*, 2023, **401**, 116361, DOI: **10.1016/j.ssi.2023.116361**.

32 M. Hofer, M. Grube, C. F. Burmeister, P. Michalowski, S. Zellmer and A. Kwade, Effective mechanochemical synthesis of sulfide solid electrolyte Li_3PS_4 in a high energy ball mill by process investigation, *Adv. Powder Technol.*, 2023, **34**(6), 104004, DOI: **10.1016/j.apt.2023.104004**.

33 R. Schlem, C. F. Burmeister, P. Michalowski, *et al.*, Energy Storage Materials for Solid-State Batteries: Design by Mechanochemistry, *Adv. Energy Mater.*, 2021, **11**(30), 2101022, DOI: **10.1002/aenm.202101022**.

34 H. Stöffler, T. Zinkevich, M. Yavuz, *et al.*, Amorphous versus Crystalline Li_3PS_4: Local Structural Changes during Synthesis and Li Ion Mobility, *J. Phys. Chem. C*, 2019, **123**(16), 10280–10290, DOI: **10.1021/acs.jpcc.9b01425**.

35 A.-C. Dippel, H.-P. Liermann, J. T. Delitz, *et al.*, Beamline P02.1 at PETRA III for high-resolution and high-energy powder diffraction, *J. Synchrotron Radiat.*, 2015, **22**(3), 675–687, DOI: **10.1107/S1600577515002222**, PMID: 25931084.

36 A. Schökel, M. Etter, A. Berghäuser, *et al.*, Multi-analyser detector (MAD) for high-resolution and high-energy powder X-ray diffraction, *J. Synchrotron Radiat.*, 2021, **28**(Pt 1), 146–157, DOI: **10.1107/S1600577520013223**, PMID: 33399563.

37 P. Juhás, T. Davis, C. L. Farrow and S. J. L. Billinge, PDFgetX3: a rapid and highly automatable program for processing powder diffraction data into total scattering pair distribution functions, *J. Appl. Crystallogr.*, 2013, **46**(2), 560–566, DOI: **10.1107/S0021889813005190**.

38 K. L. Parry, A. G. Shard, R. D. Short, R. G. White, J. D. Whittle and A. Wright, ARXPS characterisation of plasma polymerised surface chemical gradients, *Surf. Interface Anal.*, 2006, **38**(11), 1497–1504, DOI: **10.1002/sia.2400**.

39 J. H. Scofield, Hartree-Slater subshell photoionization cross-sections at 1254 and 1487 eV, *J. Electron Spectrosc. Relat. Phenom.*, 1976, **8**(2), 129–137, DOI: **10.1016/0368-2048(76)80015-1**.

40 S. Tanuma, C. J. Powell and D. R. Penn, Calculations of electron inelastic mean free paths. IX. Data for 41 elemental solids over the 50 eV to 30 keV range, *Surf. Interface Anal.*, 2011, **43**(3), 689–713, DOI: **10.1002/sia.3522**.

41 H. R. Schneider, and H. Stöffler, DE102019102589A1, 2020.

42 A. P. Thompson, H. M. Aktulga, R. Berger, *et al.*, LAMMPS – A flexible simulation tool for particle-based materials modeling at the atomic, meso, and continuum scales, *Comput. Phys. Commun.*, 2022, **271**, 108171, DOI: **10.1016/j.cpc.2021.108171**.

43 Y. Lysogorskiy, C. van der Oord, A. Bochkarev, *et al.*, Performant implementation of the atomic cluster expansion (PACE) and application to copper and silicon, *npj Comput. Mater.*, 2021, **7**(1), 97, DOI: **10.1038/s41524-021-00559-9**.

44 A. Bochkarev, Y. Lysogorskiy, S. Menon, M. Qamar, M. Mrovec and R. Drautz, Efficient parametrization of the atomic cluster expansion, *Phys. Rev. Mater.*, 2022, **6**(1), 013804, DOI: **10.1103/PhysRevMaterials.6.013804**.

45 M. Sadowski and K. Albe, Computational study of crystalline and glassy lithium thiophosphates: Structure, thermodynamic stability and transport properties, *J. Power Sources*, 2020, **478**, 229041, DOI: **10.1016/j.jpowsour.2020.229041**.

46 A. Stukowski, Visualization and analysis of atomistic simulation data with OVITO – the Open Visualization Tool, *Modell. Simul. Mater. Sci. Eng.*, 2010, **18**(1), 15012, DOI: **10.1088/0965-0393/18/1/015012**.

47 G. Kresse and J. Hafner, Ab initio molecular-dynamics simulation of the liquid-metal-amorphous-semiconductor transition in germanium, *Phys. Rev. B: Condens. Matter Mater. Phys.*, 1994, **49**(20), 14251–14269, DOI: **10.1103/physrevb.49.14251**, PMID: 10010505.

48 G. Kresse, Ab initio molecular dynamics for liquid metals, *J. Non-Cryst. Solids*, 1995, **192–193**, 222–229, DOI: **10.1016/0022-3093(95)00355-X**.

49 G. Kresse and J. Furthmüller, Efficiency of ab-initio total energy calculations for metals and semiconductors using a plane-wave basis set, *Comput. Mater. Sci.*, 1996, **6**(1), 15–50, DOI: **10.1016/0927-0256(96)00008-0**.

50 G. Kresse and J. Furthmüller, Efficient iterative schemes for ab initio total-energy calculations using a plane-wave basis set, *Phys. Rev. B: Condens. Matter Mater. Phys.*, 1996, **54**(16), 11169–11186, DOI: **10.1103/PhysRevB.54.11169**, PMID: 9984901.

51 G. Kresse and D. Joubert, From ultrasoft pseudopotentials to the projector augmented-wave method, *Phys. Rev. B: Condens. Matter Mater. Phys.*, 1999, **59**(3), 1758–1775, DOI: **10.1103/PhysRevB.59.1758**.

52 J. P. Perdew, K. Burke and M. Ernzerhof, Generalized Gradient Approximation Made Simple, *Phys. Rev. Lett.*, 1996, **77**(18), 3865–3868, DOI: **10.1103/PhysRevLett.77.3865**, PMID: 10062328.

53 X. Luo, *Interface effects in solid electrolytes for Li-ion batteries*, Karlsruher Institut für Technologie (KIT), 2022, DOI: **10.5445/IR/1000144708**.

54 M. Pompetzki and M. Jansen, Natriummonothiophosphat (V): Kristallstruktur und Natriumionenleitfähigkeit, *Z. Anorg. Allg. Chem.*, 2002, **628**(3), 641–646, DOI: **10.1002/1521-3749(200203)628:3<641::AID-ZAAC641>3.0.CO;2-8**.

55 C. Dietrich, D. A. Weber, S. J. Sedlmaier, *et al.*, Lithium ion conductivity in $Li_2S–P_2S_5$ glasses – building units and local structure evolution during the crystallization of superionic conductors $Li_3PS_4Li_7P_3S_{11}$ and $Li_4P_2S_7$, *J. Mater. Chem. A*, 2017, **5**(34), 18111–18119, DOI: **10.1039/c7ta06067j**.

56 P. Mirmira, J. Zheng, P. Ma and C. V. Amanchukwu, Importance of multimodal characterization and influence of residual Li_2S impurity in amorphous Li_3PS_4 inorganic electrolytes, *J. Mater. Chem. A*, 2021, **12**(11), 194, DOI: **10.1039/d1ta02754a**.

57 T. Scholz, F. Pielnhofer, R. Eger and B. V. Lotsch, Lanthanide orthothiophosphates revisited: single-crystal X-ray, Raman, and DFT studies of $TmPS_4$ and $YbPS_4$, *Z. Naturforsch., B: J. Chem. Sci.*, 2020, **75**(1–2), 225–231, DOI: **10.1515/znb-2019-0217**.

58 Y. Wu and W. Bensch, Syntheses, structures, and spectroscopic properties of $K_9Nd[PS_4]_4$, $K_3Nd[PS_4]_2$, $Cs_3Nd[PS_4]_2$, and $K_3Nd_3[PS_4]_4$, *Inorg. Chem.*, 2008, **47**(17), 7523–7534, DOI: **10.1021/ic800143x**, PMID: 18686946.

59 M. Tachez, J. Malugani, R. Mercier and G. Robert, Ionic conductivity of and phase transition in lithium thiophosphate Li_3PS_4, *Solid State Ionics*, 1984, **14**(3), 181–185, DOI: **10.1016/0167-2738(84)90097-3**.

60 C. Dietrich, D. A. Weber, S. Culver, *et al.*, Synthesis, Structural Characterization, and Lithium Ion Conductivity of the Lithium Thiophosphate $Li_2P_2S_6$, *Inorg. Chem.*, 2017, **56**(11), 6681–6687, DOI: **10.1021/acs.inorgchem.7b00751**, PMID: 28485931.

61 T. Yamada, S. Ito, R. Omoda, *et al.*, All Solid-State Lithium–Sulfur Battery Using a Glass-Type $P_2S_5–Li_2S$ Electrolyte: Benefits on Anode Kinetics, *J. Electrochem. Soc.*, 2015, **162**(4), A646–A651, DOI: **10.1149/2.0441504jes**.

62 C. Bischoff, K. Schuller, M. Haynes and S. W. Martin, Structural investigations of $yNa_2S + (1−y)PS_{5/2}$ glasses using Raman and infrared spectroscopies, *J. Non-Cryst. Solids*, 2012, **358**(23), 3216–3222, DOI: **10.1016/j.jnoncrysol.2012.09.023**.

63 K. S. Andrikopoulos, A. G. Kalampounias, O. Falagara and S. N. Yannopoulos, The glassy and supercooled state of elemental sulfur: vibrational modes, structure metastability, and polymer content, *J. Chem. Phys.*, 2013, **139**(12), 124501, DOI: **10.1063/1.4821592**, PMID: 24089780.

64 A. Hayashi, H. Muramatsu, T. Ohtomo, S. Hama and M. Tatsumisago, ChemInform Abstract: Improved Chemical Stability and Cyclability in $Li_2S-P_2S_5-P_2O_5-ZnO$ Composite Electrolytes for All-Solid-State Rechargeable Lithium Batteries, *J. Alloys Compd.*, 2014, **591**, 247–250, DOI: **10.1002/chin.201414010**.

65 N. Mascaraque, J. L. G. Fierro, F. Muñoz, *et al.*, Thio-oxynitride phosphate glass electrolytes prepared by mechanical milling, *J. Mater. Res.*, 2015, **30**(19), 2940–2948, DOI: **10.1557/jmr.2015.128**.

66 B. Raguž, K. Wittich and R. Glaum, Two New, Metastable Polymorphs of Lithium Pyrophosphate $Li_4P_2O_7$, *Eur. J. Inorg. Chem.*, 2019, 1688–1696, DOI: **10.1002/ejic.201801100**.

67 R. K. Brow, Review: the structure of simple phosphate glasses, *J. Non-Cryst. Solids*, 2000, **263–264**(11), 1–28, DOI: **10.1016/S0022-3093(99)00620-1**.

68 P. Glatz, M. Comte, L. Montagne, B. Doumert and L. Cormier, Quantitative determination of the phosphorus environment in lithium aluminosilicate glasses using solid-state NMR techniques, *Phys. Chem. Chem. Phys.*, 2019, **21**(33), 18370–18379, DOI: **10.1039/c9cp03181b**, PMID: 31403647.

69 A. Viani, G. Mali and P. Mácová, Investigation of amorphous and crystalline phosphates in magnesium phosphate ceramics with solid-state ^1H and ^{31}P NMR spectroscopy, *Ceram. Int.*, 2017, **43**(8), 6571–6579, DOI: **10.1016/j.ceramint.2017.02.087**.

70 D. Massiot, F. Fayon, M. Capron, *et al.*, Modelling one- and two-dimensional solid-state NMR spectra, *Magn. Reson. Chem.*, 2002, **40**(1), 70–76, DOI: **10.1002/mrc.984**.

71 S. Banerjee, M. L. Holekevi Chandrappa and S. P. Ong, Role of Critical Oxygen Concentration in the $β-Li_3PS_{4−x}O_x$ Solid Electrolyte, *ACS Appl. Energy Mater.*, 2022, **5**(1), 35–41, DOI: **10.1021/acsaem.1c03795**.